Chinese Chemical Letters 34 (2023) 107807

Contents lists available at ScienceDirect

Chinese Chemical Letters

journal homepage: www.elsevier.com/locate/cclet

Optimizing oxygen redox kinetics of M-N-C electrocatalysts *via* an *in-situ* self-sacrifice template etching strategy

Yang Yuan[a,1], Jingwen Wang[a,1], Wenbo Shi[a], Xinyi Bai[a], Ge Li[b], Zhengyu Bai[a,*], Lin Yang[a,*]

[a] School of Chemistry and Chemical Engineering, Key Laboratory of Green Chemical Media and Reaction, Ministry of Education, Collaborative Innovation Center of Henan Province for Fine Chemicals Green Manufacturing, Xinlian College, Henan Normal University, Xinxiang 453007, China
[b] Department of Mechanical Engineering, University of Alberta, 10-348 Donadeo Innovation Centre for Engineering, Edmonton, AB T6G 1H9, Canada

ARTICLE INFO

Article history:
Received 26 May 2022
Revised 18 August 2022
Accepted 2 September 2022
Available online 9 September 2022

Keywords:
Oxygen electrocatalysis
Bifunctional
Zinc-air battery
Hierarchical interconnected network
Mass transfer kinetics

ABSTRACT

The accessibility and mass transfer between catalytic sites and substrates/intermediates are essential to a catalyst's overall performance in oxygen electrocatalysis based energy devices. Here, we present an "*in-situ* self-sacrifice template etching strategy" for reconstructing MOF-derived M-N-C catalysts, which introduces micro–meso-macro pores with continuous apertures in a wide range and a central hollow-out structure to optimize the electrochemical oxygen redox kinetics. It is realized *via* one-step pyrolysis of ZIF-8 single crystal epitaxially coating on a multi-functional template of the Fe, Co co-loaded mesoporous ZnO sphere. The ZnO core is reduced during the general pyrolysis of ZIF-8 into M-N-C and acts as a pore former to etch the surrounding ZIF-8 shell into diverse channels anchoring highly exposed Fe and Co-based active sites with edge enrichment. The redesigned catalyst reveals apparent structural benefits towards enhanced oxygen redox kinetics as bifunctional cathode catalysts of rechargeable zinc-air battery compared with the primitive bulk M-N-C catalysts and the mixture of commercial Pt/C and Ir/C. The unique structure-based activity advantages, the omitted template removal step and good template compatibility during synthesis make the strategy universal for the channel engineering of electrocatalysts.

The development of carbon-based non-noble metal catalysts for electrochemical oxygen redox is a promising way to counter the increasing energy and environmental challenge nowadays. In particular, non-noble metals embedded on N-doped C materials (M-N-Cs) are talented candidates to replace the costly Pt-, Ir-, and Ru-based commercial oxygen electrocatalysts [1–3]. The M-N-C catalysts are not only abundantly reserved but also potential multi-activity through rational modulation towards both oxygen reduction and evolution reactions (ORR and OER), which makes them more desirable in rechargeable energy devices such as metal-air batteries [4,5]. Up to now, both the isolated N-coordinated metal atoms and the encapsulated metallic nanoparticles in carbon-based catalysts are reported as efficient oxygen electrocatalytic sites in alkaline zinc-air batteries [6–9]. However, in the kinetic process of oxygen electrocatalysis, the accessibility and mass transfer between these actives sites and the electrolyte is of equal significance to ensure the rapid and continuous interaction on the solid-liquid-gas interface. Hence, structural modulation of the M-N-C catalysts is still urgent.

On the one hand, pore engineering, especially based on traditional template methods, is widely used in size and shape modulation of porosity. Channels derived from organic and inorganic templates with specific sizes, such as silicon-, polystyrene-based pore former, are always fascinating for the well-aligned aperture [10–11]. In terms of oxygen electrocatalysis, however, hierarchically apertures in continuous ranges tend to be more effective in kinetic mass transfer [12–14]. The interconnected structures of micro-pores and meso-/macro-pores manifest efficient synergy for both the exposure of active sites and reactant/products toward or away from them. Additionally, not only the heterogeneity between templates and precursors but also the high concentration of acid, base or organic reagent for subsequent template removal would likely lead to quality degradation of the finally porous products.

On the other hand, metal-organic frameworks (MOFs) have been served as a feasible precursor for pyrolysis into M-N-C catalysts because the removal of low thermal-stable metal nodes (such as zinc, magnesium and indium) creates abundantly pyrolytic micro-pores and extensive surface area which greatly contributes to full exposure of the inside metal active sites [15]. Meanwhile, MOFs are also flexible for anchoring and dispersing

* Corresponding authors.
E-mail addresses: baizhengyu@htu.edu.cn (Z. Bai), yanglin1819@163.com (L. Yang).
[1] These authors contributed equally to this work.

https://doi.org/10.1016/j.cclet.2022.107807
1001-8417/

various metal cations for pyrolyzing into tunable types of active sites such as isolated atoms and encapsulated nanoparticles. However the monotonous micro-porosity is deficient for rapid mass transport.

Thus, in order to achieve ideal M-N-C catalysts for both active site exposure and efficient mass transfer. Herein, we design an *in-situ* self-sacrifice template etching strategy to compile individual advantages in pore construction of template methods and MOF pyrolysis. Firstly, meso–porous ZnO sphere is employed as a self-sacrifice template. With ligands etching and recombining with Zn^{2+}, a ZIF-8 single-crystal is easily epitaxial on it as a self-template precursor. Then, the ZnO serves for multi-intention: (1) It is a highly effective pore former during pyrolysis to *in-situ* etch the ZIF-8 derived carbon supports, fabricate graphitic defects, interconnect the inherent micro-pores by newly formed abundant meso– and macro-pores, and (2) simultaneously vacate the hollow-out cage further increasing the external surface. Additionally, (3) its meso–porosity is beneficial for loading and isolating active metal species. In this way, a highly accessible bimetallic FeCo-N-C network is successfully achieved. It possesses not only single-atoms and bimetallic nanoparticles as bifunctional active sites but also micro-, meso–, macro-pores and hollow-out cage interconnected hierarchical networks for efficient kinetic mass transfer towards ORR, OER and air cathodes performance in rechargeable zinc-air batteries.

The self-sacrifice template etching strategy is illustrated in Fig. 1a. The preparation of meso–porous ZnO spheres and the epitaxial growth of ZIF-8 precursors are modified according to references and detailed in Supporting Information [16]. In particular, a special vacuum pretreatment to the reactant solution is processed to promote the entry and confinement of the active metallic acetylacetonates ($Fe(acac)_3$ and $Co(acac)_2$) in ZnO channels, which is expected to alleviate the serious aggregation in pyrolysis (Fig. S1 in Supporting information). After achieving the precursors loaded with $Fe(acac)_3$ and $Co(acac)_2$ (noted as ZnO@ZIF-8), the self-sacrifice template etching process is executed during pyrolyzing the precursors into M-N-C catalysts. In this process, the reduced zinc species from ZnO templates melt and etch the ZIF-8 shell. Finally, all zinc species are removed by heating up to their boiling point of about 907 °C, and the ZnO@ZIF-8 precursors are derived into the hierarchical interconnected FeCo-N-C catalysts [17]. In the well-tailored structure, the abundant micro-pores contributed by ZIF-8 pyrolysis and other hierarchical pores by self-sacrifice template etching strategy are successfully integrated. With this strategy, we fabricate a bifunctional catalyst endowed with highly accessible Fe- and Co-based bimetallic active sites, noted as FeCo-N-C-hierarchical, for efficiently kinetic oxygen redox. The catalyst derived from a ZIF-8 bulk precursor (noted as FeCo-N-C-bulk) is synthesized as a control group to highlight the effects of well-designed pore engineering.

Subsequently, we employ FeCo-N-C-hierarchical as the model to analysis its hierarchical porosity and impacts on kinetic modulation of oxygen electrocatalysis. The morphological and structural properties of FeCo-N-C-hierarchical are characterized by micrology and spectroscopy. The multi-functional spherical ZnO templates and the ZnO@ZIF-8 precursors are showed in Figs. 1b-d and Fig. S2 (Supporting information), respectively, proving their successfully synthesized. In the SEM images, the catalyst particles inherit the truncated octahedron geometry of ZIF-8 single crystal (Fig. S3 in Supporting information). During pyrolysis, the ZIF-8 frameworks derive into rough carbon supports with slight shrinkage of volume size. It is worth to note that the achievement of self-sacrifice template etching process is showed as not only a hollow-out central nave in the TEM image (Fig. 1e) but also several channels ex-

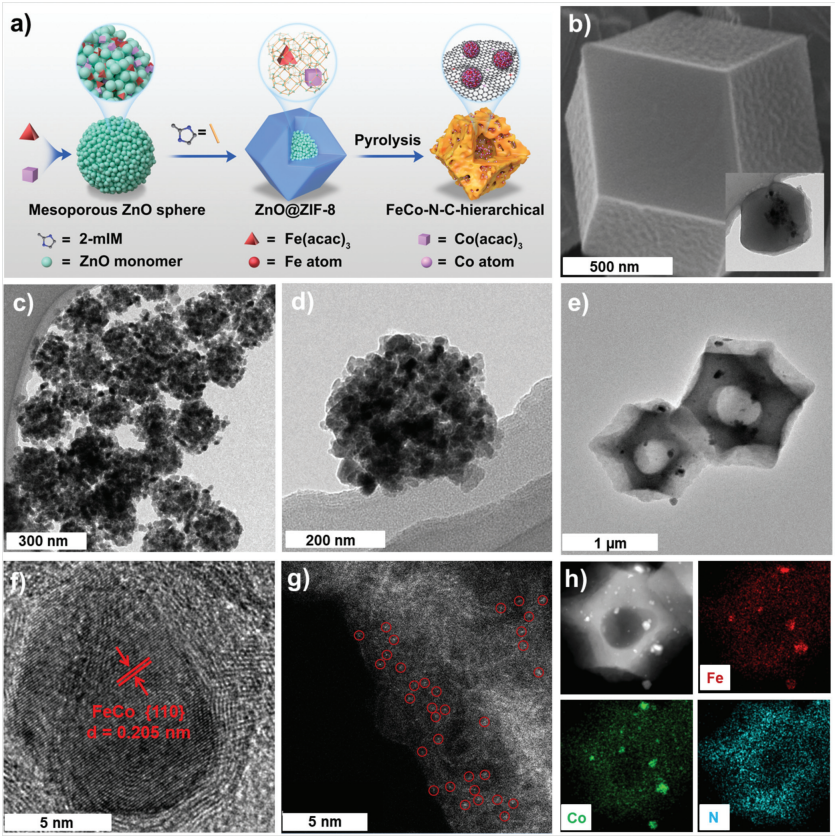

Fig. 1. (a) Illustration for the "self-sacrifice template etching strategy". SEM and TEM images of (b) ZnO@ZIF-8; (c, d) meso–porous ZnO spheres and (e) FeCo-N-C-hierarchical. (f, g) HR-TEM, HAADF-STEM images of representative areas in FeCo-N-C-hierarchical and (h) elemental mapping images of a representative catalyst.

tending to the particle surface (marked with orange cycles in Fig. S3). In contrary, the catalyst particle derived from ZIF-8 only reveals a dense structure (Figs. S4 and S5 in Supporting information). This unique structure of FeCo-N-C-hierarchical is likely to boost the electrolyte accessing the overall catalyst particle during electrocatalytic processes. The large central hollow-out volume is benefited from the occupying and oxidizing effects of ZnO template to the surrounding carbon substrates [18]. To detect the metal species in the catalyst, high-resolution transmission microscopy (HR-TEM) and the aberration correction high angle annular dark field scan transmission electron microscopy (AC-HAADF-STEM) are employed for a typical section of the catalyst (Figs. 1f and g). In Fig. 1f, the motif of a nanoparticle encapsulated by graphitic carbon is observed. The lattice stripe is determined as 2.05 Å, which attributed to the {110} plane of FeCo alloy [19]. Fig. 1g showed the existence of single atomic metal sites as evenly dispersing spots (a part of them are circled out for clarity). On the elemental mapping images (Fig. 1h), part of Fe and Co signal converges at the location of highlight spots and the rest reveals uniformly dispersing. This is in accordance with the distribution of Fe and Co elements in alloy particles and single atoms observed in Figs. 1f and g, respectively. Furthermore, it also reveals abundant and uniform N signals throughout the catalyst. With XPS spectra in the spectroscopy analysis section below, pyridine-, pyrrole-, graphitic- and metallic-N are detected, which reveals the abundant N-doped graphitic motif in the catalyst. Combined with the characteristic peaks of oxidized Fe and Co in their 2p spectra (Fig. S6 in Supporting information), the metallic-N can be specified to FeN_x and CoN_x species. Both the encapsulated bimetallic nanoparticles and the isolated FeN_x and CoN_x sites embedded on abundant N-doped graphitic carbon are desired active sites in ORR and OER [20–26].

Spectroscopy measurements are used to comprehensively analyze the N-doped graphitic supports and metal sites in the catalyst. The PXRD pattern of the bulk ZIF-8 precursor only reveals the peaks in agreement with its simulated curves, while, the ZnO@ZIF-8 reveals the diffractial peaks of ZIF-8 and ZnO simultaneously, which indicates the successfully epitaxial template composite of the ZnO@ZIF-8 precursor (Fig. 2a). The final FeCo-N-C-hierarchical catalyst reveals the characteristic peak assigning to FeCo {110} plane (PDF #49–1567), which verifies the FeCo alloy nanoparticles in the TEM images [19]. The absence of ZnO peaks reveals its removal during the self-sacrifice template etching process through calcination. The broad peak assigned to the {002} facet of graphitic carbon is also observed [7]. The Raman spectrum of FeCo-N-C-hierarchical reveals a higher I_D/I_G value of 1.07 than that of FeCo-N-C-bulk (1.03) (Fig. 2b). Furthermore, the significantly increased area ratio of the D1/G peaks is observed. The D1 peak at about 1350 cm^{-1} is attributed to the vibration mode at edges of the graphitic crystallites [13]. The larger $area_{D1}/area_G$ (1.38) indicates that with the ZnO self-sacrifice template etching effect, FeCo-N-C-hierarchical possesses a more edge-enrichment graphitic support than that of the FeCo-N-C- bulk control group ($area_{D1}/area_G = 1.22$) (Fig. 2b). The high- resolution XPS analysis for N 1s orbit reveals the co-existence of pyridine- (398.6 eV), pyrrole- (400.4 eV), graphitic- (401.2 eV), oxidic- (402.3 eV) and metal-N (399.4 eV) (Figs. 2c and d) [27]. Lower graphitic-N ratio against the total of unsaturated pyridine- and pyrrole-N is manifested in FeCo-N-C-hierarchical than FeCo-N-C-bulk. It implies under the self-sacrifice template etching treatment, FeCo-N-C-hierarchical possesses a more porous graphitic scaffold with edge defects, which is beneficial for the ORR and OER process [28,29]. Additionally, the Fe $2p_{3/2}$ orbit analysis detects the signals at about 707.6 eV, 710.7 eV and 712.9 eV, which are corresponding to Fe^0, Fe^{2+} and Fe^{3+}, respectively (Fig. S6) [30]. Likewise, the Co $2p_{3/2}$ plot can be assigned to Co^0 (778.9 eV), Co^{2+} (782.5) and Co^{3+} (780.6 eV). [31,32] The positive and zero valence states are corresponding to the metal species of FeN_x, CoN_x and FeCo nanoparticles in the catalyst, respectively [7,33].

N_2 adsorption-desorption isotherms are conducted to evaluate the pore structure treated by the self-sacrifice template etching strategy (Figs. 2e and f). FeCo-N-C-bulk possesses mainly adsorption amount contributed by micro- and macro-pores in the relative pressure range (P/P_0) before 0.01 and after 0.9, respectively. In contrast, an extra hysteresis loop for the desorbed isotherm of FeCo-N-C-hierarchical is clearly observed in the region above $P/P_0 > 0.4$. It definitely indicates the meso–pores exist inside the FeCo-N-C-hierarchical particles. As the BET surface area is specifically contributed by micro-porosity, the decrease of FeCo-N-C-hierarchical (701 m^2/g) than that of FeCo-N-C-bulk (948 m^2/g) implies a formative process that a part of the original micro-pores derived from pyrolysis of the ZIF-8 shell is *in-situ* transformed into larger pores through the etching effect. It is specified in the pore size distribution examined by fitting to the NLDFT models (Fig. 2f). The micropore distribution of FeCo-N-C-hierarchical at about 1 nm is slightly lower than FeCo-N-C-bulk. However, in the subsequent wide region (1–40 nm), various apertures are distributed continuously in

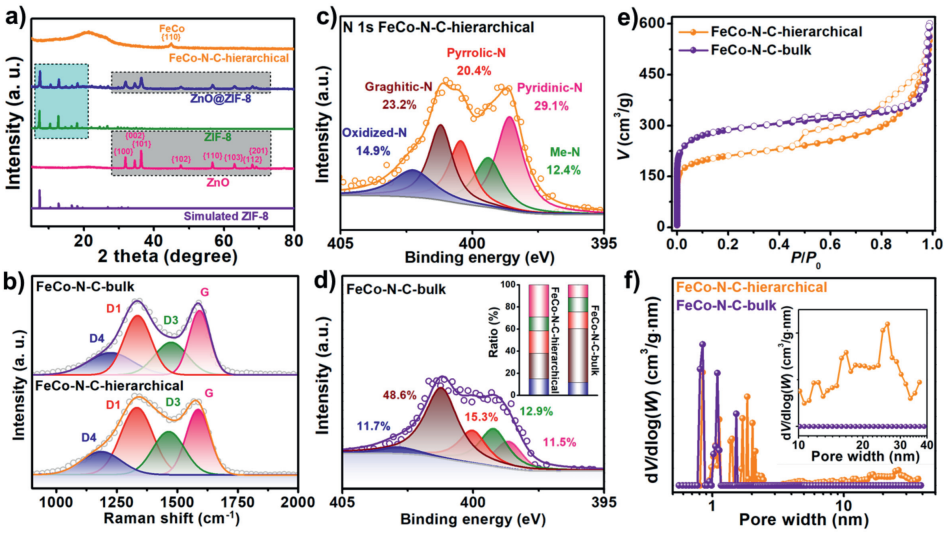

Fig. 2. (a) PXRD, (b) Raman spectra, (c, d) N 1s high-resolution XPS curves for each synthesized catalyst, inset of (d) is N species distribution, colar code: blue, oxidized-N; wine, graphitic-N; red, pyrrolic-N; olive, metal-N; pink, pyridinic-N. (e) 77 K N_2 adsorption-desorption isotherms, and (f) pore-size distribution.

FeCo-N-C-hierarchical, which indicates the existence of abundant mesopores (Fig. 2f, inset). This continuous distribution of hierarchical interconnected network is beneficial not only to the exposure of active sites, but also to the kinetic mass transfer process on spatial and time scale during catalysis [13].

The unique channel structural advantages of the catalyst inspire us to further investigate its facilitation for electrochemical oxygen redox kinetics. The ORR and OER performances are first evaluated by employing a typical three-electrode system. Fig. 3a is the ORR linear sweep voltammetry (LSV) curve of each catalyst under 1600 rpm. The FeCo-N-C-hierarchical prepared with the 1:1 Fe/Co ratio in raw materials (noted as FeCo(1:1)-N-C-hierarchical) reveals the superior limited current density (–5.8 mA/cm^2 at 0.7 V *vs.* RHE) and half-wave potential ($E_{1/2}$) (0.84 V *vs.* RHE) among FeCo(2:1)-N-C-hierarchical (–5.3 mA/cm^2 and 0.84 V *vs.* RHE), FeCo(1:2)-N-C-hierarchical (–5.8 mA/cm^2 and 0.82 V *vs.* RHE) and the bulk catalyst (FeCo-N-C-bulk) derived from the primitive ZIF-8 precursor (–5.1 mA/cm^2 and 0.82 V *vs.* RHE). Although the $E_{1/2}$ of FeCo-N-C-hierarchical catalysts are lower than that of commercial Pt/C counterpart (0.88 V *vs.* RHE), it can be seen as a strong dependency with their differences in onset potential, which corresponds to the intrinsic activity of the catalytic sites. To investigate their kinetic activity, we further calculate the tafel slopes. Much smaller values for the FeCo-N-C-hierarchical catalysts are exhibited than that of the bulk catalyst and commercial Pt/C (Fig. 3b). It indicates their structural advantages for kinetic mass transfer. We select FeCo(1:1)-N-C-hierarchical as the target catalyst owing to its best comprehensive performance shown in Fig. S7f (Supporting information). Fig. S7a (Supporting information) reveals its LSV curves under various rpm from 400 to 2025. The K-L curves derived from it show a desired 4-electron transfer path for ORR in a wide potential range of 0.3–0.7 V *vs.* RHE (Fig. S7b in Supporting information). Fig. S7c (Supporting information) exhibits its higher stability than that of Pt/C. It shows only a 9% decrease under a high potential of 0.84 V *vs.* RHE after 41,000 s.

The OER activities of the catalysts are also compared by the LSV curves and derived tafel slopes. In Fig. 3c, FeCo(1:1)-N-C-hierarchical reveals steepest current increasing and the smallest overpotential of 323 mV at 10 mA/cm^2. Its structural benefits for kinetic mass transfer and active site accessibility during OER are evaluated by comparing the tafel slope and electrochemically active surface area (EASA) with FeCo-N-C-bulk [34]. A much smaller tafel slope (82 mV/dec) and greater double-layer capacitance (C_{dl}) (16.0 mF/cm^2) than that of FeCo-N-C-bulk (182 mV/dec and 2.7 mF/cm^2) is detected (Figs. 3d and e). The charge-transfer resistance (R_{ct}) (10.1 Ω) is also smaller than that of FeCo-N-C-bulk (40.5 Ω) as shown in the electrochemical impedance spectroscopy (EIS) (Fig. S7e in Supporting information). The smaller ORR and OER tafel slopes, the higher C_{dl} and the lower R_{ct} of FeCo-N-C-hierarchical than FeCo-N-C-bulk highlight the well-designed structural advantages for fast kinetics in electrocatalytic oxygen redox (Table S3 in Supporting information). During the OER process, the carbon corrosion commonly occurs on carbon-based catalysts [35]. Therefore, we detect the OER Faradaic efficiency at various potentials from 1.3 V to 1.6 V, which shows slightly higher than that of the commercial Ir/C control group (Fig. S7i in Supporting information). Additionally, FeCo-N-C-hierarchical also possesses longer durability than the commercial control groups as well as a comparable potential gap of 0.703 V between $E_{1/2}$ and $E_{j=10}$ to the efficient catalysts reported recently (Fig. 3f, Fig. S7d and Table S4 in Supporting information). To identify the active site contributions for catalyzing ORR and OER, we prepared control catalysts which mainly contain FeN_x, CoN_x and both of them as active sites, respectively. Their ORR and OER LSV curves show that the FeN_x, CoN_x sites mainly contribute to ORR activity by revealing comparable $E_{1/2}$ and j_{limit} with FeCo-N-C-hierarchical which contain FeN_x, CoN_x and FeCo nanoparticles (Fig. S7g in Supporting information). On the counterpart, the introduction of FeCo nanoparticles enhances the OER activity as seen by its considerable decrease of $\eta_{j=10}$ comparing against the prepared catalysts (Fig. S7h in Supporting information). In virtue of these advantages above, we further estimate its performance as the cathode catalyst of zinc-air batteries (ZABs).

Rechargeable flow ZABs are assembled with FeCo-N-C-hierarchical or Pt/C&Ir/C 1:1 mixture coating on a gas diffusion layer as the air cathode, respectively. The battery model is detailed in Fig. 4a and Fig. S11 (Supporting information). A normal open current voltage for FeCo-N-C-hierarchical (1.49 V) based ZAB is observed (Fig. S9 in Supporting information). Fig. 4b shows the polarization curves. The FeCo-N-C-hierarchical based ZAB reveals comparable charging and higher discharging voltages than that of Pt/C&Ir/C, illuminating a better activity. The maximum power density is calculated as 129.0 mW/cm^2 at 168.2 mA/cm^2, which is higher than Pt/C&Ir/C (113.5 mW/cm^2 at 160.5 mA/cm^2) and FeCo-N-C-bulk (103.6 mW/cm^2 at 123.8 mA/cm^2) (Fig. S12 in Supporting information). The specific capacitances are calculated by long-time galvanostatic discharge curves at 5 mA/cm^2 (Fig. 4c). FeCo-N-C-hierarchical based ZAB shows higher specific capacitance of 782.1 mAh/g_{Zn} than that of Pt/C&Ir/C (772.7 mAh/g_{Zn}) and

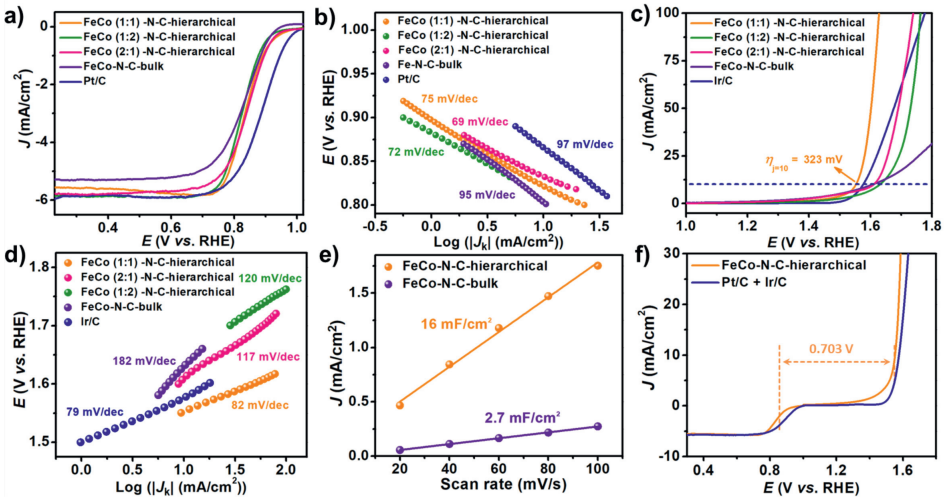

Fig. 3. Electrochemical performance comparison of the catalysts: (a) ORR LSV curves under O_2 saturated 0.1 mol/L KOH at 1600 rpm and (b) derived tafel slopes; (c) OER LSV curves under N_2 saturated 1 mol/L KOH at 1600 rpm and (d) derived tafel slopes; (e) charging current density-rpm curves and (f) overall polarization plots.

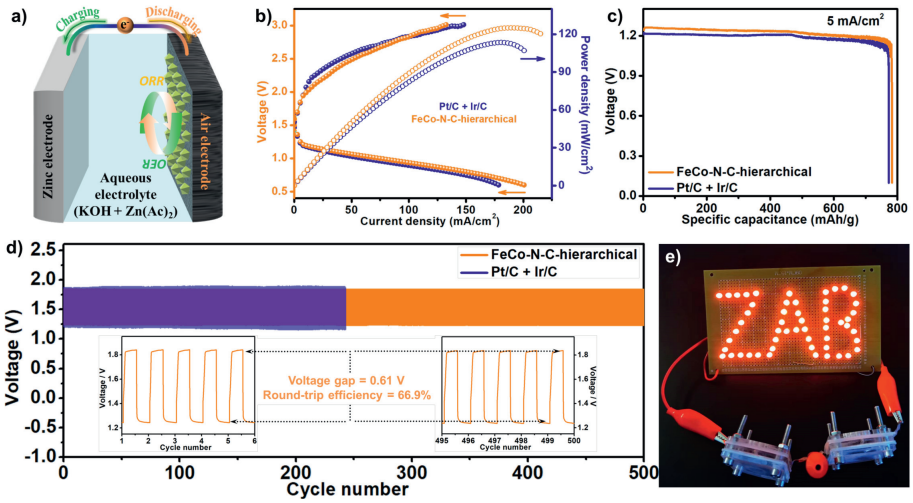

Fig. 4. (a) a model for the homemade zinc-air battery; (b) polarization and power density curves, (c) specific capacity plots derived from the long-time galvanostatic discharge curves at 5 mA/cm^2 according to the consumed Zn plates at anode and (d) galvanostatic discharge-charge cycling curves at 5 mA/cm^2 of the ZABs based on FeCo-N-C-hierarchical and Pt/C+Ir/C catalysts. (e) A "ZAB" LED screen powered by FeCo-N-C-hierarchical based batteries.

FeCo-N-C-bulk (760.0 mAh/g_{Zn}). The cyclic stabilities are measured by 5 mA/cm^2 charging/discharging galvanostatic tests (Fig. 4d). The FeCo-N-C-hierarchical group shows a charge/discharge voltage of 1.85 and 1.24 V with a short voltage gap of 0.61 V. Furthermore, the catalyst can maintain its morphology and the battery can keep a round-trip efficiency of 66.9% after a cyclic process of more than 250 h and 500 cycles, better than that of Pt/C&Ir/C (62.1% at the 241th cycle) (Figs. S3c and S10 in Supporting information). Fig. 4e shows that a 2.8 V light-emitting diodes (LEDs) screen can be lightened by two FeCo-N-C-hierarchical based batteries in series.

In summary, with a well-designed "self-sacrifice template etching strategy", we successfully construct continuous micro–meso-macro-pore and hollow-out interconnected networks in FeCo-N-C-hierarchical catalysts. Our developed catalyst reveals structure-related rapid oxygen redox kinetics. This study provides a new path towards pore engineering of M-N-C materials for solid-liquid-gas catalysis.

Declaration of competing interest

The authors declare no competing financial interest.

Acknowledgments

This work was financially supported by the National Natural Science Foundation of China (Nos. 51922008, 52072114 and 51872075), the 111 Project (No. D17007), Henan Center for Outstanding Overseas Scientists (No. GZS2022017), and Xinxiang Major Science and Technology Projects (No. 21ZD001).

Supplementary materials

Supplementary material associated with this article can be found, in the online version, at doi:10.1016/j.cclet.2022.107807.

References

[1] C.X. Zhao, B.Q. Li, J.N. Liu, Q. Zhang, Angew. Chem. Int. Ed. 60 (2021) 4448–4463.
[2] G. Wu, A. Santandreu, W. Kellogg, et al., Nano Energy 29 (2016) 83–110.
[3] C.X. Zhao, J.N. Liu, J. Wang, et al., Chem. Soc. Rev. 50 (2021) 7745–7778.
[4] A. Kundu, S. Mallick, S. Ghora, C.R. Raj, ACS Appl. Mater. Interfaces 13 (2021) 40172–40199.
[5] J. Fu, R. Liang, G. Liu, et al., Adv. Mater. 31 (2019) 1805230.
[6] F. Dong, M. Wu, Z. Chen, et al., Nano-Micro Lett. 14 (2021) 36.
[7] Q. Zhang, P. Liu, X. Fu, et al., Adv. Funct. Mater. 32 (2022) 2112805.
[8] M. Wu, G. Zhang, Y. Hu, et al., Carbon Energy 3 (2020) 176–187.
[9] Z. Bai, Y.P. Deng, Z. Chen, Sci. Bull. 65 (2020) 1511–1513.
[10] K. Shen, L. Zhang, X. Chen, et al., Science 359 (2018) 206–210.
[11] E. Doustkhah, R. Hassandoost, A. Khataee, R. Luque, M.H.N. Assadi, Chem. Soc. Rev. 50 (2021) 2927–2953.
[12] H. Zhao, Y. Zhang, L. Li, Chin. Chem. Lett. 32 (2021) 140–145.
[13] L.Soo Hong, K. Jiheon, C.Dong Young, et al., J. Am. Chem. Soc. 141 (2019) 2035–2045.
[14] F. Chang, P. Su, U. Guharoy, et al., Chin. Chem. Lett. 34 (2023) 107462.
[15] G. Cai, P. Yan, L. Zhang, H.C. Zhou, H.L. Jiang, Chem. Rev. 121 (2021) 12278–12326.
[16] Y. Ma, X. Wang, X. Sun, et al., Inorg. Chem. Front. 7 (2020) 1046–1053.
[17] H. Zhang, S. Hwang, M. Wang, et al., J. Am. Chem. Soc. 139 (2017) 14143–14149.
[18] S. Liu, M. Wang, X. Yang, et al., Angew. Chem. Int. Ed. 59 (2020) 21698–21705.
[19] S.H. Yin, J. Yang, Y. Han, et al., Angew. Chem. Int. Ed. 59 (2020) 21976–21979.
[20] W. Li, B. Liu, D. Liu, et al., Adv. Mater. 34 (2022) 2109605.
[21] Y. Xiong, Y. Yang, F.J. DiSalvo, H.D. Abruña, J. Am. Chem. Soc. 141 (2019) 10744–10750.
[22] Z. Liang, H. Guo, H. Lei, R. Cao, Chin. Chem. Lett. 33 (2022) 3999–4002.
[23] J. Chen, H. Li, C. Fan, et al., Adv. Mater. 32 (2020) 2003134.
[24] W. Zhang, Y. Chao, W. Zhang, et al., Adv. Mater. 33 (2021) 2102576.
[25] R. Li, D. Wang, Adv. Energy Mater. 12 (2022) 2103564.
[26] H. Li, Y. Wen, M. Jiang, et al., Adv. Funct. Mater. 31 (2021) 2011289.
[27] F. Jaouen, J. Herranz, M. Lefevre, et al., ACS Appl. Mater. Interfaces 1 (2009) 1623–1639.
[28] X. Fu, N. Li, B. Ren, et al., Adv. Energy Mater. 9 (2019) 1803737.
[29] M. Xiao, Z. Xing, Z. Jin, et al., Adv. Mater. 32 (2020) e2004900.
[30] Y. Du, L. Liu, Y.K. Li, et al., New J. Chem. 46 (2022) 8271–8276.
[31] G. Zhang, P. Wang, W.T. Lu, et al., ACS Appl. Mater. Interfaces 9 (2017) 28566–28576.
[32] G. Zhang, W. Lu, F. Cao, Z. Xiao, X. Zheng, J. Power Sources 302 (2016) 114–125.
[33] Z. Lei, Y. Tan, Z. Zhang, et al., Nano Res. 14 (2020) 868–878.
[34] Z. Zhang, X. Zhao, S. Xi, et al., Adv. Energy Mater. 10 (2020) 2002896.
[35] S. Yin, G. Li, X. Qu, et al., ACS Appl. Energy Mater. 3 (2020) 625–634.